Barriers to front propagation in laminar, three-dimensional fluid flows

Minh Doan,[1,*] JJ Simons,[1] Katherine Lilienthal,[1] Tom Solomon,[1,†] and Kevin A. Mitchell[2,‡]

[1] *Department of Physics and Astronomy, Bucknell University, Lewisburg, PA 17837, USA*
[2] *School of Natural Sciences, University of California, Merced, CA 95344, USA*

(Dated: February 5, 2018)

We present the first experiments on one-way barriers that block reaction fronts in a fully three-dimensional (3D) fluid flow. Fluorescent Belousov-Zhabotinsky reaction fronts are imaged with laser-scanning in a laminar, overlapping vortex flow. The barriers are analyzed with a 3D extension to burning invariant manifold (BIM) theory that was previously applied to 2D advection-reaction-diffusion processes. We discover tube and sheet barriers that guide the front evolution. The experimentally-determined barriers are explained by BIMs calculated from a model of the flow.

PACS numbers: 82.40.Ck, 47.52.+j, 47.10.Fg, 47.70.Fw

I. INTRODUCTION

Numerous chemical, biological, atmospheric and oceanic processes are characterized by the propagation of a front that separates two different phases. In many of these processes, the front propagation is strongly affected by fluid flows in the system. This generalized advection-reaction-diffusion (ARD) problem [1, 2] has applications in a wide variety of systems, including microfluidic reactors [3, 4]; cellular- and embryonic-scale biological processes [5]; oceanic-scale algal blooms [6, 7]; and the propagation of a disease in a mobile society [8]. Previous experiments [9–12] have identified dynamically-defined, one-way barriers that block reaction fronts propagating in a wide range of two-dimensional (2D), laminar flows. These barriers have been explained theoretically [9, 13–16] as *burning invariant manifolds* (BIMs) that are generalizations of passive invariant manifolds [17–21] that impede passive mixing in a flow. But most ARD processes involve flows that are three-dimensional (3D). The question of whether BIMs can be generalized to 3D flows is important toward developing a comprehensive theory of front propagation in ARD systems.

In this article, we present the first experimental study of front propagation in a laminar, 3D fluid flow, along with an extension of the BIM theory to account for the additional spatial dimension. The extension from 2D to 3D raises several topological questions: (1) Are there generalized BIMs that also act as barriers for moving reaction fronts in 3D flows? (2) What is the topology of these barriers – if they exist – for a 3D flow? (3) Are the barriers one-way, similar to their 2D counterparts? (4) How does the structure of these barriers depend on the flow and reaction-diffusion front speeds?

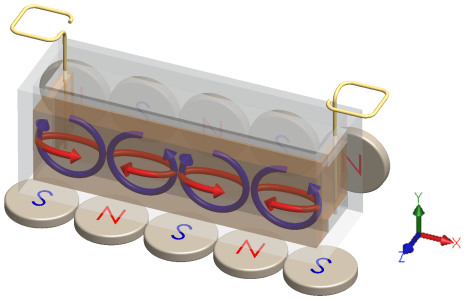

FIG. 1: (Color online) Fluid cell, showing the magnetohydrodynamic forcing and the resulting flow formed from the superposition of a horizontal (red) and vertical (blue) chain of vortices. The fluid channel measures 0.80 cm x 8.0 cm horizontally with a height of 1.9 cm.

II. EXPERIMENTAL SETUP

The flow is a superposition of horizontal and vertical vortex chains, generated experimentally using a magnetohydrodynamic technique (Fig. 1). An electrical current passes lengthwise through fluid in an optical-quality quartz cell. The current interacts with a magnetic field produced by two chains of five 3/4" Nd-Fe-Bo magnets, one below and the other behind the cell. The magnets below the cell produce the horizontal vortex chain and the magnets behind produce the vertical vortices. The bottom and side magnets are aligned so that the superposed vortex chains line up.

The fluid in the cell is composed of the chemicals used for the excitable Ruthenium (Ru)-catalyzed Belousov-Zhabotinsky (BZ) reaction[22–24]. The Ru indicator is initially in its orange, reduced state, but when triggered (either naturally or by inserting a silver wire), the indicator is oxidized, producing a green, pulse-like, autocatalytic reaction front that propagates with a speed $V_0 = 70\mu m/s$ in the absence of a flow. The electrical current and imposed electrical field (< 0.1 V/cm) are small enough to avoid significant effects on the front propagation speed [25]. Measurements of front speeds without an electrical current also indicate a negligible effect from

*current address: Department of Mechanical Engineering, Keio University, 3-14-1 Hiyoshi, Kohoku-ku, Yokohama, Kanagawa, 223-8522,Japan. Email:mndoan@keio.jp
†Electronic address: tsolomon@bucknell.edu
‡Electronic address: kmitchell@ucmerced.edu

the permanent magnets [26]. We also neglect curvature effects on front speeds [1].

Three-dimensional BZ patterns have been imaged previously[27], but only for stagnant systems. These are the first experiments to obtain full 3D imaging of the time-evolution of BZ reaction fronts in a fluid flow. We employ a scanning, laser imaging technique that uses fluorescence of reduced (but not oxidized) Ru indicator. A 400-mW, 405 nm laser beam is reflected off a pair of voltage-controlled mirrors. One mirror oscillates rapidly, causing the beam to scan horizontally through the cell; the other mirror scans through 50 different heights in the cell. For each height, the fluorescence of the reduced Ru is imaged from above with an sCMOS video camera. The result is a stack of 50 images which can be reconstructed into a full 3D view of the evolving reaction front.

Particle image velocimetry (PIV) is used to characterize the flow. We model the flow as the superposition of two vortex chains described by streamfunctions

$$\begin{aligned}\psi_1(x,y,z) &= -\frac{1}{\pi}\cos(\pi x)W(y)f(z),\\ \psi_2(x,y,z) &= -\frac{1}{\pi}\cos(\pi x)W(z)g(y).\end{aligned} \tag{1}$$

The velocity field is derived from these streamfunctions via $u_x(x,y,z) = \partial\psi_1/\partial y + \partial\psi_2/\partial z$, $u_y(x,y,z) = -\partial\psi_1/\partial x$, and $u_z(x,y,z) = -\partial\psi_2/\partial x$. In Eq. (1), $f(z) = 0.5(1 + 0.5[1 + \cos(2\pi z)])$ and $g(y) = a(y + 0.5)\exp[-b(y + 0.5)] + c$ (with a=46, b=7.8 and c=0.9) are taper functions (fitted to the PIV data) to account for variation of the vortex strengths with distance from the magnets. The function W [28] depends on the boundary conditions at the side and top/bottom surfaces. In the simplest case with free-slip boundary conditions,

$$W(y) = \cos(\pi y). \tag{2}$$

In this paper, we use more realistic no-slip boundary conditions [28], with

$$\begin{aligned}W(y) = &\cos(q_0 y) - A_1\cosh(q_1 y)\cos(q_2 y) +\\ &A_2\sinh(q_1 y)\sin(q_2 y),\end{aligned} \tag{3}$$

with $q_0 = 3.973638032476331$, $q_1 = 5.194998480822572$, $q_2 = 2.125929469473915$, $A_1 = 0.061508353836287$, and $A_2 = 0.103869826106854$. In Eq. (1), the xyz-coordinates are non-dimensionalized by the vortex length, height, and width, so that a single vortex occupies a unit cell. Similarly, the resulting fluid velocities are non-dimensionalized by the maximum velocity of the second vortex chain.

We define a dimensionless front propagation speed $v_0 \equiv V_0/U$, where U is the maximum (dimensionful) fluid velocity of the second vortex chain. Note that there is no advective (passive) transport between adjacent vortices in this flow.

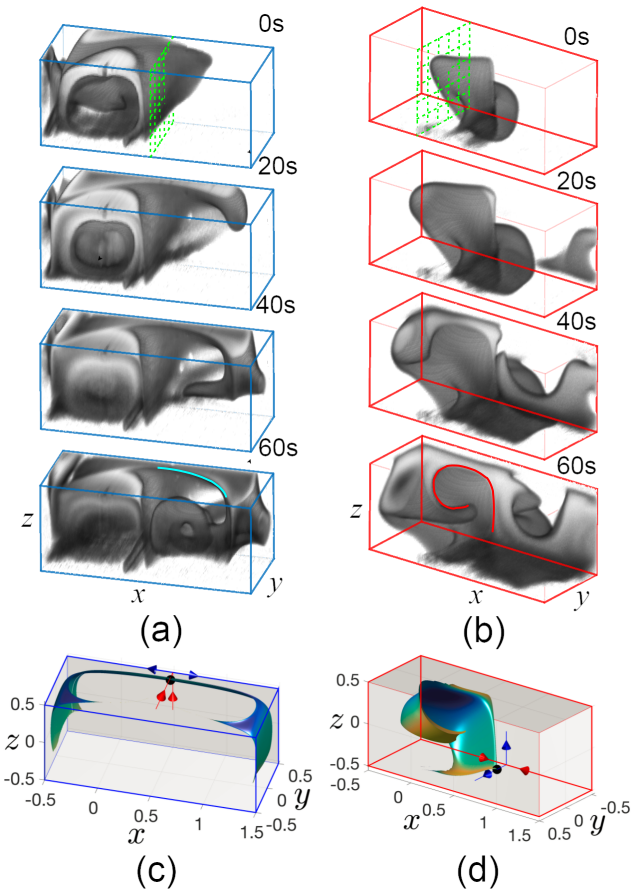

FIG. 2: (Color online) Sequences showing the evolution of reaction fronts for the middle two unit cells (4.0 cm) of the overlapping vortex flow. (a) $v_0 = 0.064$; the evolving front (viewed at an angle from above) is blocked by a quarter-tube, arch-like barrier that spans two vortices. The leading edge of this barrier is shown as a cyan curve in the 60 s image. (b) $v_0 = 0.16$; the evolving front (viewed at an angle from below) is blocked by a scroll-shaped, sheet barrier, the edge of which is shown in red in the 60 s image. Movies of these sequences can be found online in Supplemental Material [29]. (c) and (d) Simulated burning invariant manifolds corresponding to the barriers seen in (a) and (b). The dots show the burning fixed points to which the BIMs are attached. The red (blue) arrows show the stable (unstable) directions of the fluid flow near the advective fixed point. A rotating animation of the theoretical BIM in (d) (in the Supplemental Material [29]) better illustrates its 3D nature.

III. THREE-DIMENSIONAL IMAGING RESULTS

Examples of evolving reaction fronts are shown in Fig. 2. Two of the most dominant barriers are shown in these sequences: a quarter-tube barrier that follows an edge of the unit cell and forms an arch that spans two neighboring vortices (Fig. 2a) and a large sheet-like barrier that forms near the boundary between neighboring vortices (Fig. 2b). Reactions propagating in a partic-

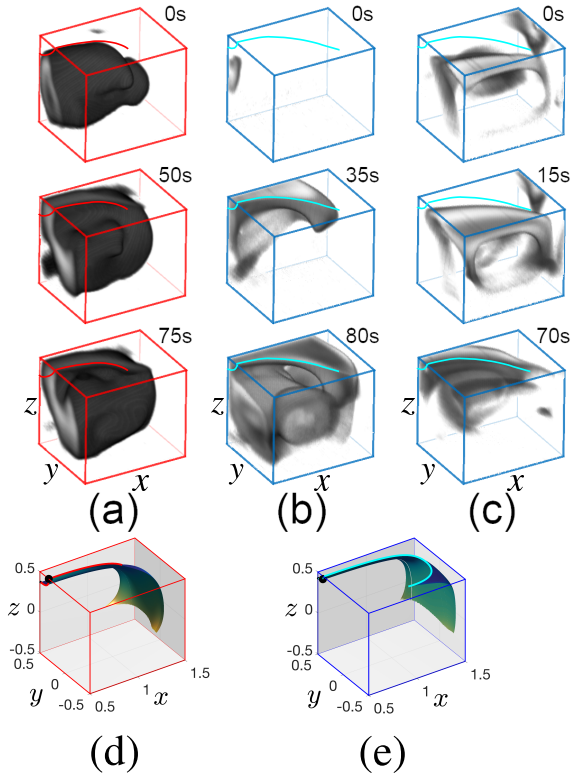

FIG. 3: (Color online) Part of the quarter-tube, arch-like barrier. (a) $v_0 = 0.16$; (b) and (c) $v_0 = 0.064$. The front left surface corresponds to the green grid in Fig. 2(a). In (a) and (b), the front enters the quarter-tube from the back and is blocked by the tube-barrier as it moves in the $-y$ direction near the top surface. In (c), a front moving in the $+y$ direction near the top penetrates into the quarter-tube. Panels (d) and (e) show numerically computed BIMs corresponding to the same viewing region and v_0 as columns a and b/c. An animation of the BIM in (d) is given in Supplemental Materials [29].

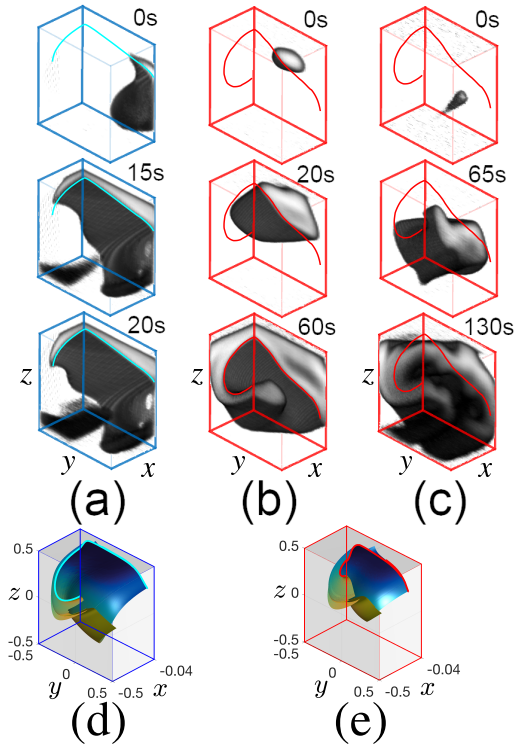

FIG. 4: (Color online) Part of the sheet (scroll) barrier. (a) $v_0 = 0.064$; (b) and (c) $v_0 = 0.16$. The front right surface corresponds to the green grid in Fig. 2(b). In (a) and (b), a front above the barrier (partially drawn in cyan and red curves) is blocked from propagating downward by the barrier. In (c), a front propagating upward passes through the (one-way) barrier. Panels (d) and (e) show numerically computed BIMs corresponding to the same viewing region and v_0 as columns a and b/c. Compared to Fig. 2 (d), part of a second BIM has also been plotted near $y = -0.5$.

ular direction do not penetrate through these barriers but must circumnavigate them, similar to reaction barriers observed in previous 2D experiments. Note that the sheet-like barrier (Fig. 2b) wraps into the left vortex. A reaction front going to the left passes the advective separatrix between the vortices, hits the vertical part of this barrier and wraps around over the top of the vortex. The front penetrates into the center of the left vortex only because the barrier itself scrolls into the center.

Convergence of the experimental reaction fronts and the one-way nature of these barriers can be seen in Figs. 3 and 4. Column (b) of both of these figures shows fronts converging on – but not passing through – part of a BIM, while column (c) shows fronts penetrating through the BIMs in the opposite direction.

The locations of these barriers also depend on the non-dimensional front propagation speed v_0, also shown in Figs. 3 and 4. The barriers are farther away from the vortex boundaries (where passive invariant manifolds reside) and closer to the vortex centers for larger v_0.

The topology of the barriers can be qualitatively understood by considering the Eulerian fixed points of the simple free-slip flow given by Eq. (1) with W in Eq. (2). The eight corners of each vortex cell are hyperbolic fixed points with either two stable and one unstable directions (SSU) or one stable and two unstable directions (SUU). If triggered near an SSU fixed point (Fig. 5a), a reaction front will flow outward with the unstable direction; it will also propagate outward *against* the two stable directions, until balanced by the incoming flow, where $|\mathbf{u}| = v_0$. The result is a tube-like, one-way barrier (Fig. 5a) that confines reactions propagating outward, but allows reactions propagating inward to penetrate the tube.

If triggered near an SUU fixed point (Fig. 5b), the reaction will flow outward along the two unstable directions and will also propagate outward against the single stable direction until balanced by the incoming flow, $|\mathbf{u}| = v_0$. The result is two one-way sheet barriers (Fig. 5b), each of which blocks reactions going away from the SUU fixed

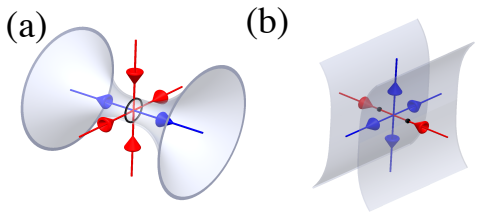

FIG. 5: (Color online) (a) Cartoon of a tube-like reaction barrier expected near an advective fixed point with SSU stability and equal stable flow rates. (b) Cartoon of sheet-like reaction barriers expected near an SUU fixed point.

point.

IV. BURNING INVARIANT MANIFOLD THEORETICAL ANALYSIS

To quantitatively analyze the behavior of reaction fronts in a 3D flow, we extend the previous 2D BIM theory [9–16], in which we directly model the motion of an infinitesimal element of the reaction front. In 2D, a front element is parameterized by two spatial coordinates and a single orientation angle. In 3D, a minimal model requires three spatial dimensions and two orientation angles. However, it is computationally easier to characterize the orientation of a front element using the three xyz-components of its unit normal vector $\mathbf{n}$. The result is a 6D set of ODEs (with the 5D system embedded as the invariant subspace $|\mathbf{n}| = 1$):

$$\frac{dr_i}{dt} = u_i + v_0 n_i, \tag{4a}$$

$$\frac{dn_i}{dt} = n_i \sum_{j,k} u_{j,k} n_j n_k - \sum_j u_{j,i} n_j, \quad i,j,k = x,y,z, \tag{4b}$$

where u_i and n_i are the components of the fluid velocity field and unit normal, respectively, and $u_{j,k}$ is the partial derivative of u_j in the k direction. The first equation denotes motion of the front element due to advection (first term) and burning, i.e., propagation of the front relative to the fluid in the normal direction (second term). The second equation denotes rotation of the front element due to the flow. A formal derivation of Eqs. (4) is given by Oberlack and Cheviakov [30]. We provide an intuitive geometric derivation of Eq. (4b) in Appendix A 1.

A *burning fixed point* is a position $\mathbf{r}$ and orientation $\mathbf{n}$ where $d\mathbf{r}/dt = d\mathbf{n}/dt = 0$ in Eqs. (4). According to the prior Fig. 5 discussion, these often occur near advective fixed points, with two burning fixed points near an SUU point and a circle of fixed points near an SSU point (with equal unstable flow rates). See the black dots in Fig. 5. The BIMs are calculated by integrating trajectories of Eq. (4) away from the burning fixed points.

For comparison to the experiments, we use no-slip boundary conditions, Eq. (3). Though the number and positions of the burning fixed points are different from what we would get for the free-slip case given by $W(z)$ in Eq. (2), the same computational approach generates the BIMs; see Figs. 2c and 2d. Computational details are given in the Appendix. The online Supplemental Material [29] contains rotating animations of BIMs that better visualize their 3D nature. The BIM in Fig. 2c is a quarter tube that flairs out away from the burning fixed point (black dot), forming an arch that mimics the experimental barrier in Fig. 2a. It also matches one quarter of the cartoon in Fig. 5a, since the BIM in Fig. 2c surrounds an SSU advective fixed point on the edge of the domain. The quarter-tube geometry is especially clear in the cross-section Fig. 3e, which corresponds to the experiments in Figs. 3b and 3c. Similarly, Fig. 3d shows the BIM cross-section for the larger v_0 value, corresponding to Fig. 3a. Note that the larger v_0 produces a fatter tube, as in the experiments.

Though the tube BIM only blocks reactions propagating outward, it can still act as a trip-wire for reactions initiated outside the tube. A front that encounters a tube BIM penetrates inside but then is trapped by the outward-blocking nature of the BIM; see Fig. 3b, in which a reaction triggered below the back of the tube penetrates into the BIM but is stopped by the outward-blocking BIM as the front moves in the $-y$ direction near the top. The one-way nature of the theoretical BIMs is demonstrated in the supplemental movies [29]; a burst of trajectories moving outward from a single location are blocked by or pass through the BIM depending on whether the point is behind or in front of the BIM, respectively.

Comparing the numerical BIM in Fig. 2d to the experiment in Fig. 2b, they both exhibit the same scroll behavior. Near the boundary between the two vortices, Fig. 2d also resembles the cartoon in Fig. 5b, having a flat sheet-like surface normal to the fluid inflow direction $\hat{\mathbf{x}}$. Figures 4d and 4e show cross-sections of the scroll BIM for the two v_0 values, comparable to the experiments in Figs. 4a and 4b/c. Each theory figure actually shows two BIMs, so close together they appear as one: the original BIM from Fig. 2 and a second BIM in the gap between the original BIM and the front left surface. As seen by the red and cyan intersection curves, these BIMs show the same scroll structure as the experiments, including the fact that the larger v_0 value creates a BIM closer to the vortex center. For both the tube and scroll, the experimental and theoretical BIMs differ in their detailed structure. But this is to be expected given the simple analytical form of the fluid velocity field Eq. (1).

There are more BIMs in this system than observed in these experiments. For example, symmetry dictates that the BIM in Fig. 2d reflects about the midplane to a second BIM on the right. However, this BIM is not seen in Fig. 2b because the reaction fronts pass through it in the allowed direction.

V. CONCLUSIONS

In summary, we experimentally visualized one-way barriers that block the motion of reaction fronts in a truly 3D laboratory-scale fluid flow. We developed a 3D extension of the burning invariant manifold theory, used previously only in 2D, which provides a theoretical explanation and framework for studying these reaction barriers. Using an explicit form of the flow field, direct numerical computation shows that the shape of the BIMs captures the essential geometry of the experimentally measured barriers. This theory applies to much more than chemical reactions; given any flow and any process that produces a sharp propagation front (with zero-flow propagation speed V_0), the BIMs predicted by Eqs. (4) will identify one-way barriers that impede the motion of that front. Ultimately, the success of the BIM approach for identifying reaction front barriers in both 2D and now 3D flows suggests that this approach could form the basis for a more comprehensive theory of front propagation in fluid flows.

Acknowledgments

These studies were supported by the US National Science Foundation under grants DMR-1361881, DUE-1317446, PHY-0748828, and CMMI-1201236. We would like to thank Jack Raup, Moises Veloz and Joe Tolman for assistance with the milling of the apparatus. KAM would like to thank Marcos Mendoza for initial discussions on the 3D theory of BIMs.

Appendix A: Theory details

1. Derivation of the front element dynamics

We provide a simple geometric derivation of Eq. (4b); Eq. (4a) is obvious. See Ref. [30] for a formal derivation of these equations using the G-equation. Fig. 6 shows the front element as a small rectangle tangent to the front, with normal vector $\mathbf{n}$. We introduce instantaneous unit vectors $\mathbf{e}_1$ and $\mathbf{e}_2$, spanning the tangent rectangle, so that $(\mathbf{e}_1, \mathbf{e}_2, \mathbf{e}_3)$ forms an orthonormal frame, with $\mathbf{e}_3 = \mathbf{n}$. The tangent rectangle evolves with the fluid, i.e. $\mathbf{e}_1$ and $\mathbf{e}_2$ evolve as tangent vectors

$$\dot{e}_{1i} = \sum_j u_{i,j} e_{1j}, \quad \dot{e}_{2i} = \sum_j u_{i,j} e_{2j}, \quad i,j = x,y,z. \tag{A1}$$

However, $\mathbf{n} = \mathbf{e}_1 \times \mathbf{e}_2$ does not evolve as a tangent vector. Rather,

$$\dot{\mathbf{n}} = \dot{\mathbf{e}}_1 \times \mathbf{e}_2 + \mathbf{e}_1 \times \dot{\mathbf{e}}_2 - \mathbf{n}(\dot{\mathbf{e}}_1 \cdot \mathbf{e}_1 + \dot{\mathbf{e}}_2 \cdot \mathbf{e}_2), \tag{A2}$$

where the first two terms follow from the product rule and the final terms, which do not change the direction of $\mathbf{n}$,

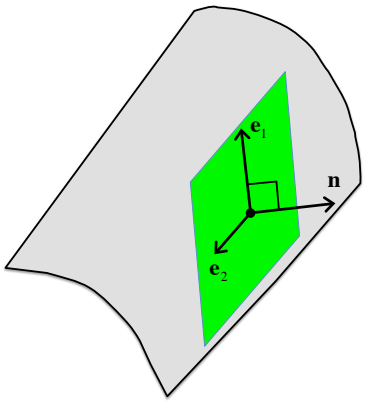

FIG. 6: (Color online) A front element with normal vector $\mathbf{n}$ and tangent vectors $\mathbf{e}_1$ and $\mathbf{e}_2$.

simply enforce the requirement that $|\mathbf{n}| = 1$. Taking the components of Eq. (A2) with respect to the $(\mathbf{e}_1, \mathbf{e}_2, \mathbf{e}_3)$ basis, we find

$$\dot{n}_1 = \mathbf{e}_1 \cdot \dot{\mathbf{n}} = \mathbf{e}_1 \cdot (\dot{\mathbf{e}}_1 \times \mathbf{e}_2) = -\mathbf{e}_3 \cdot \dot{\mathbf{e}}_1 = -u_{3,1}, \tag{A3}$$

and similarly

$$\dot{n}_2 = -u_{3,2}. \tag{A4}$$

Finally,

$$\begin{aligned} \dot{n}_3 &= \mathbf{e}_3 \cdot \dot{\mathbf{n}} \\ &= \mathbf{e}_3 \cdot (\dot{\mathbf{e}}_1 \times \mathbf{e}_2) + \mathbf{e}_3 \cdot (\mathbf{e}_1 \times \dot{\mathbf{e}}_2) - (\dot{\mathbf{e}}_1 \cdot \mathbf{e}_1 + \dot{\mathbf{e}}_2 \cdot \mathbf{e}_2) \\ &= 0. \end{aligned} \tag{A5}$$

When Eq. (4b) is evaluated in the same $(\mathbf{e}_1, \mathbf{e}_2, \mathbf{e}_3)$ basis, one obtains the exact same results as Eqs. (A3)-(A5), thereby establishing its validity.

2. A stable form of the front element dynamics

The front element dynamics Eqs. (4) preserve the length of the unit normal, i.e. $n = |\mathbf{n}| = 1$ is conserved. This follows immediately from

$$\frac{d(n^2)}{dt} = 2(n^2 - 1)(\mathbf{n} \cdot \nabla \mathbf{u}\, \mathbf{n}), \tag{A6}$$

which follows from Eq. (4b). However, the condition $n = 1$ can be either stable or unstable, depending on whether $\mathbf{n} \cdot \nabla \mathbf{u}\, \mathbf{n}$ is positive or negative. A more robust formulation of the front element dynamics is given by

$$\frac{dr_i}{dt} = u_i + v_0 \frac{n_i}{n}, \tag{A7a}$$

$$\frac{dn_i}{dt} = n_i \sum_{j,k} u_{j,k} n_j n_k - n^2 \sum_j u_{j,i} n_j, \quad i,j,k = x,y,z. \tag{A7b}$$

These equations are identical to Eqs. (4) when $n = 1$, but differ crucially when $n \neq 1$, since it now holds that

$$\frac{d(n^2)}{dt} = 0. \tag{A8}$$

Thus, the condition $n = 1$ is now (neutrally) stable to small perturbations. Furthermore, by explicitly dividing by n in Eq. (A7a), dr_i/dt is insensitive to any small deviation from $n = 1$. For these reasons, Eqs. (A7) are the preferred method to actually compute front element trajectories.

3. Computing burning fixed points

A burning fixed point $(\mathbf{r}, \mathbf{n})$ is a point for which Eqs. (A7), or equivalently Eqs. (4), equal zero and for which $|\mathbf{n}| = 1$. Both conditions can be satisfied by instead solving the equations

$$0 = u_i + v_0 n_i, \tag{A9a}$$

$$0 = n_i \sum_{j,k} u_{j,k} n_j n_k - n^2 \sum_j u_{j,i} n_j + (n^2 - 1) n_i, \tag{A9b}$$

which we do using Newton's method as follows. First, a necessary condition for a burning fixed point to occur is that the fluid velocity u must equal the burning velocity v_0. We thus identify the level set in xyz-space for which the constraint $|\mathbf{u}(x, y, z)| = v_0$ holds. See Fig. 7a. Points are then randomly selected on this constraint surface, and for each point $\mathbf{r}_0$ the unit normal is set to $\mathbf{n}_0 = -\mathbf{u}(\mathbf{r}_0)/v_0$. The phase space point $(\mathbf{r}_0, \mathbf{n}_0)$ is then used as an initial seed in Newton's method to solve Eqs. (A9). The resulting fixed points are shown as the (blue) dots and (green) triangles in Fig. 7a.

4. Computing burning invariant manifolds

The stability of each fixed point is found by computing the Jacobian matrix of Eq. (A7) using finite difference. The tangent vector $(\mathbf{v}_r, \mathbf{v}_n) = (0, \mathbf{n})$ is always an eigenvector of the Jacobian matrix. But this eigenvector points perpendicular to the physically relevant constraint surface $|\mathbf{n}| = 1$, and is thus ignored. We thus restrict the space of tangent vectors $(\mathbf{v}_r, \mathbf{v}_n)$ to

$$\mathbf{v}_n \cdot \mathbf{n} = 0. \tag{A10}$$

Furthermore, it turns out that any vector $(\mathbf{v}_r, \mathbf{v}_n)$ at the fixed point that is tangent to a BIM must also satisfy

$$\mathbf{v}_r \cdot \mathbf{n} = 0. \tag{A11}$$

We thus focus on the four-dimensional subspace satisfying both Eqs. (A10) and (A11). Since we are seeking two-dimensional unstable BIMs, we find those fixed points that have exactly two unstable directions in this 4D subspace. These are distinguished as the (blue) dots in Fig. 7a. The (green) triangles are any other fixed points.

To compute the quarter-tube BIM (for $v_0 = 0.16$), we compute the two-dimensional unstable manifold connected to the (blue dot) fixed point $\mathbf{r}_u$ near $(.5, .5, .5)$. To do this, we first integrate the unstable manifold in the least unstable eigendirection. This creates a heteroclinic (red) curve in the plane $x = 0.5$, connecting the (blue) dot $\mathbf{r}_u$ to the (green) triangle $\mathbf{r}_s$ in Fig. 7b. We then perturb this curve slightly in the positive x-direction and use the perturbed points as a set of initial conditions for integrating the unstable surface in the remaining direction. This creates the middle (blue) swath of the unstable manifold in Fig. 7b. However, the two (green and yellow) slivers of the unstable manifold on either side of the blue swath must be computed separately. These two slivers connect the blue swath to the walls of the fluid cell. To compute these remaining slivers, we first compute their intersections with the cell wall.

Consider the front element dynamics restricted to one of the boundary planes of the experimental cell; let $\mathbf{a}$ denote the normal vector to this boundary. Within the boundary, the fluid velocity field $\mathbf{u}$ is everywhere tangent to the boundary. We may thus apply the 2D theory of BIMs within this plane. It was shown in Ref. [16] that the BIMs for a 2D, time-independent fluid flow must be solutions to the differential equation below (with one of the two choices of sign):

$$\frac{d\mathbf{r}}{dt} = \left[1 - \frac{v_0^2}{u^2}\right] \mathbf{u} \pm \frac{v_0}{u} \sqrt{\left(1 - \frac{v_0^2}{u^2}\right)} \mathbf{u}^\perp, \tag{A12}$$

where $\mathbf{u}^\perp$ is the vector $\mathbf{u}$ rotated by $\pi/2$, i.e. $\mathbf{u}^\perp = \mathbf{a} \times \mathbf{u}$. Applying Eq. (A12) to the plane $y = 0.5$, with $\mathbf{a} = \hat{\mathbf{y}}$, we integrate away from the fixed point $\mathbf{r}_s$, creating the black curve on the back side of the cell $y = 0.5$ of Fig. 7b. We then perturb the black curve slightly into the interior of the cell, and integrate these points away from the boundary using the full 6D Eqs. (A7). This sweeps out the green sliver in Fig. 7b. A similar approach is used to integrate the black curve emanating from $\mathbf{r}_u$ within the plane $z = 0.5$ and to sweep out the yellow sliver in Fig. 7b.

Each trajectory on the BIM is stopped once it reaches a sufficient length or it reaches a cusp in the surface. Finally, after points along the BIM are computed, they are triangulated to create a surface for display purposes.

The scroll BIM is computed in a similar fashion. See Fig. 7c. The fixed point $\mathbf{r}_u$ in Fig. 7c is the same as the (blue) dot near $(.5, -.5, -.5)$ in Fig. 7a. The red curve emanating upward from $\mathbf{r}_u$ is the unstable manifold in the plane $x = 0.5$. Part of this curve is shifted slightly to the left and integrated to construct the blue wedge in Fig. 7c. The remaining (green) wedge of the unstable manifold is computed by first computing the black curve in the plane $z = -0.5$ using Eq. (A12), perturbing this curve upward, and then sweeping out the (green) manifold.

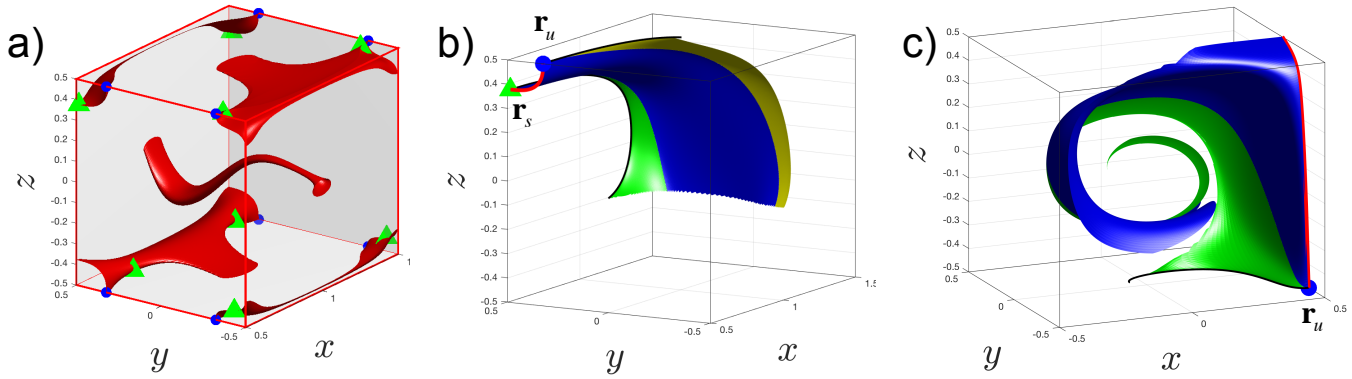

FIG. 7: (Color online) a) The surface (red) at which $v_0 = |\mathbf{u}|$ for $v_0 = 0.16$ and $\mathbf{u}$ given by Eqs. (1) and (3). There are eight burning fixed points with two unstable BIM directions (blue circles) and eight burning fixed points with other stability types (green triangles). b) The quarter-tube BIM. c) The scroll BIM.

The quarter-tube and scroll BIMs for $v_0 = 0.064$ were computed in a similar manner to the above.

[1] Z. Neufeld and E. Hernandez-Garcia, *Chemical and Biological Processes in Fluid Flows: A Dynamical Systems Approach* (Imperial College Press, 2009).
[2] A. Tzella and J. Vanneste, Phys. Rev. E **90**, 011001(R) (2014).
[3] T. John and I. Mezic, Phys. Fluids **19** (2007).
[4] C. L. A. Berli and P. A. Kler, Microfluid Nanofluid **20**, 104 (2016).
[5] P. K. Trong, J. Guck, and R. E. Goldstein, Phys. Rev. Lett. **109**, 028104 (2012).
[6] E. Hernandez-Garcia and C. Lopez, Ecol. Complexity **1**, 253 (2004).
[7] D. Bastine and U. Feudel, Nonlinear Processes in Geophysics **17**, 715 (2010).
[8] J. Ge, K. I. Kim, Z. Lin, and H. Zhu, J. Differential Equations **259**, 5486 (2015).
[9] J. Mahoney, D. Bargteil, M. Kingsbury, K. Mitchell, and T. Solomon, Europhys. Lett. **98**, 44005 (2012).
[10] D. Bargteil and T. Solomon, Chaos **22**, 094107 (2012).
[11] P. W. Megson, M. L. Najarian, K. E. Lilienthal, and T. H. Solomon, Phys. Fluids **27**, 023601 (2015).
[12] S. Gowen and T. Solomon, Chaos **25**, 087403 (2015).
[13] K. A. Mitchell and J. R. Mahoney, Chaos **22**, 037104 (2012).
[14] J. R. Mahoney and K. A. Mitchell, Chaos **23**, 043106 (2013).
[15] J. R. Mahoney and K. A. Mitchell, Chaos **25**, 087404 (2015).
[16] J. R. Mahoney, J. Li, C. Boyer, T. Solomon, and K. A. Mitchell, Phys. Rev. E **92**, 063005 (2015).
[17] R. S. MacKay, J. D. Meiss, and I. C. Percival, Physica D **13**, 55 (1984).
[18] V. Rom-Kedar, Nonlinearity **7**, 441 (1994).
[19] T. H. Solomon, S. Tomas, and J. L. Warner, Phys. Rev. Lett. **77**, 2682 (1996).
[20] G. Haller, Physics of Fluids **13**, 3365 (2001).
[21] G. A. Voth, G. Haller, and J. P. Gollub, Phys. Rev. Lett. **88**, 254501 (2002).
[22] S. K. Scott, *Oscillations, Waves, and Chaos in Chemical Kinetics* (Oxford University Press, Oxford, 1994).
[23] R. Kapral and E. K. Showalter, *Chemical Waves and Patterns* (Kluwer, Dordrecht, Netherlands, 1995).
[24] Initial concentrations of the reactants for each run are: [BrMA] = 0.09 M, [MA] = 0.03 M, $[BrO_3^-]$ = 0.16 M, $[H_2SO_4]$ = 0.25 M, $[(Ru(bpy)_3)^{2+}]$ = 0.3 mM.
[25] M. Pornprompanya, S. C. Muller, and H. Seveikovaa, Phys. Chem. Chem. Phys. **4**, 3370 (2002).
[26] H. Okano and H. Kitahata, Bioelectromagnetics **34**, 220 (2013).
[27] J. Tamás Bánsági and O. Steinbock, Chaos **18**, 026102 (2008).
[28] S. Chandresekhar, *Hydrodynamic and Hydromagnetic Stability* (Clarendon, Oxford, 1961).
[29] See Supplemental Material at (URL will be inserted by publisher) for movies of the evolving experimental fronts and movies of the theoretical BIMs.
[30] M. Oberlack and A. F. Cheviakov, J. Eng. Math. **66**, 121 (2010).